

ARTICLE

Open Access

Universal point spread function engineering for 3D optical information processing

Md Sadman Sakib Rahman^{1,2,3} and Aydogan Ozcan^{1,2,3}  

Abstract

Point spread function (PSF) engineering has been pivotal in the remarkable progress made in high-resolution imaging in the last decades. However, the diversity in PSF structures attainable through existing engineering methods is limited. Here, we report universal PSF engineering, demonstrating a method to synthesize an arbitrary set of spatially varying 3D PSFs between the input and output volumes of a spatially incoherent diffractive processor composed of cascaded transmissive surfaces. We rigorously analyze the PSF engineering capabilities of such diffractive processors within the diffraction limit of light and provide numerical demonstrations of unique imaging capabilities, such as snapshot 3D multispectral imaging without involving any spectral filters, axial scanning or digital reconstruction steps, which is enabled by the spatial and spectral engineering of 3D PSFs. Our framework and analysis would be important for future advancements in computational imaging, sensing, and diffractive processing of 3D optical information.

Introduction

The spreading or blurring of a point source of light by an optical system is described by its point spread function (PSF)¹. PSF engineering², which involves the purposeful design of the PSF of an optical system, offers a powerful tool for optical imaging and microscopy^{3–6}. For example, 3D localization microscopy has greatly benefitted from PSF engineering, enabling remarkable precision in emitter localization^{7–10}. PSF engineering is also important for optical data storage and the design of telescopes^{11,12}, among many other applications. Therefore, the ability to intricately manipulate or optimize PSFs holds great promise for improvements in the design of optical systems. PSF engineering is usually implemented by placing an appropriately designed phase mask at the pupil (Fourier) plane, which results in a laterally invariant PSF whose functional form remains the same (ideally) as the emitting point source moves laterally over the object plane. However, the spectral and axial variations of such PSFs have been utilized for improved performance in 3D localization microscopy^{10,13,14}. An optical system that can also control

and engineer laterally varying PSFs, matching a desired set of functions, could provide new degrees of freedom for better imaging performance, especially for task-specific^{15–18} imaging and sensing systems.

Diffractive optical processors, comprising successive optimized diffractive surfaces that modulate the amplitude and/or the phase of the incident light waves¹⁹, have emerged as a powerful tool for passive manipulation of light²⁰. In this framework, the task-specific optimization of the spatial distribution of diffractive features over the constituent surfaces is performed using deep learning tools on a digital forward model. Following this optimization, the resulting surfaces are fabricated and assembled to form the physical diffractive device, which performs its intended task all-optically through passive light–matter interactions as the input light propagates through a thin volume, typically spanning only a few hundred wavelengths. Such diffractive processors, also known as diffractive optical networks or diffractive networks, have been used for diverse applications ranging from all-optical classification to phase-imaging, optical encryption/decryption, display, and 3D imaging, among others^{19,21–26}. Capable of performing universal linear transformations, such diffractive processors have also been shown to synthesize arbitrarily chosen spatially and spectrally varying 2D PSFs between the input and output planes^{27–30};

Correspondence: Aydogan Ozcan (ozcan@ucla.edu)

¹Electrical and Computer Engineering Department, University of California, Los Angeles, CA, USA

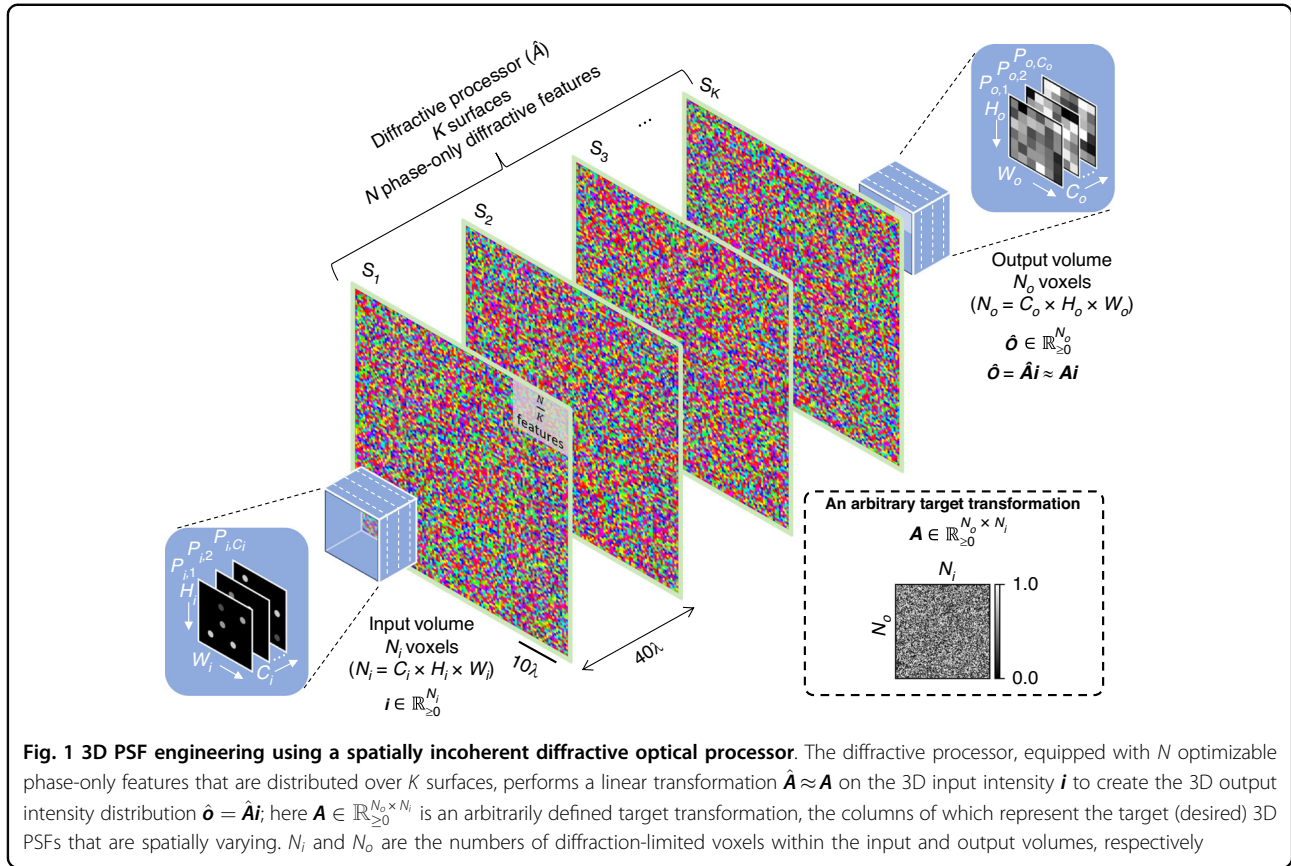
²Bioengineering Department, University of California, Los Angeles, CA, USA

Full list of author information is available at the end of the article

© The Author(s) 2025



Open Access This article is licensed under a Creative Commons Attribution 4.0 International License, which permits use, sharing, adaptation, distribution and reproduction in any medium or format, as long as you give appropriate credit to the original author(s) and the source, provide a link to the Creative Commons licence, and indicate if changes were made. The images or other third party material in this article are included in the article's Creative Commons licence, unless indicated otherwise in a credit line to the material. If material is not included in the article's Creative Commons licence and your intended use is not permitted by statutory regulation or exceeds the permitted use, you will need to obtain permission directly from the copyright holder. To view a copy of this licence, visit <http://creativecommons.org/licenses/by/4.0/>.



however, there have been no studies on 3D PSF engineering using diffractive processors, which is highly important in the context of 3D optical information processing.

Here, we report universal 3D PSF engineering with spatially incoherent diffractive processors, showing that such optical processors can synthesize an arbitrarily defined (desired) set of 3D diffraction-limited PSFs between the voxels of an input volume and an output volume, given that sufficient design degrees of freedom (i.e., diffractive features) are available for optimization. We analyze the effect of diffraction limit on the 3D information processing capacity of diffractive networks and numerically demonstrate a novel application of 3D PSF engineering, namely, snapshot 3D imaging without any digital postprocessing. We also demonstrate *spectrally and spatially* varying 3D PSF engineering for snapshot multispectral 3D imaging, also without the need for any digital postprocessing.

The unique contributions of this work include: (1) the demonstration of universal linear processing of 3D optical information using spatially incoherent monochrome diffractive optical networks, accurately performing any arbitrary (desired) set of spatially varying 3D PSFs; (2) the demonstration of spectrally multiplexed 3D optical

information processing with spatially and spectrally programmed 3D incoherent PSFs; and (3) the application of such spatially and spectrally varying 3D incoherent PSFs for snapshot 3D multispectral imaging of a volume of emitters using a single output detector array, i.e., without any spectral filters, axial scanning or digital reconstruction steps needed. Our analyses and results are significant for future developments in computational imaging, sensing, and diffractive processing of 3D optical information, such as optical data storage and 3D microscopy.

Results

In this Article, we use the terms ‘diffractive processor’ and ‘diffractive network’ interchangeably. Figure 1 presents the schematic of a spatially incoherent diffractive network that synthesizes an arbitrary set of spatially varying 3D PSFs, defined between the input and output volumes. The input volume is assumed to comprise C_i discrete planes, each of which is discretized into $H_i \times W_i$ diffraction-limited ($\sim \lambda/2$) pixels. Specifically, the lateral discretization interval of the input volume is assumed to be 0.53λ , whereas the axial discretization interval (same as the plane-to-plane distance, d_{pp} , introduced later in the manuscript) is assumed to be 2.67λ , unless otherwise stated. The vector $\mathbf{i} \in \mathbb{R}_{\geq 0}^{N_i}$ represents the distribution of

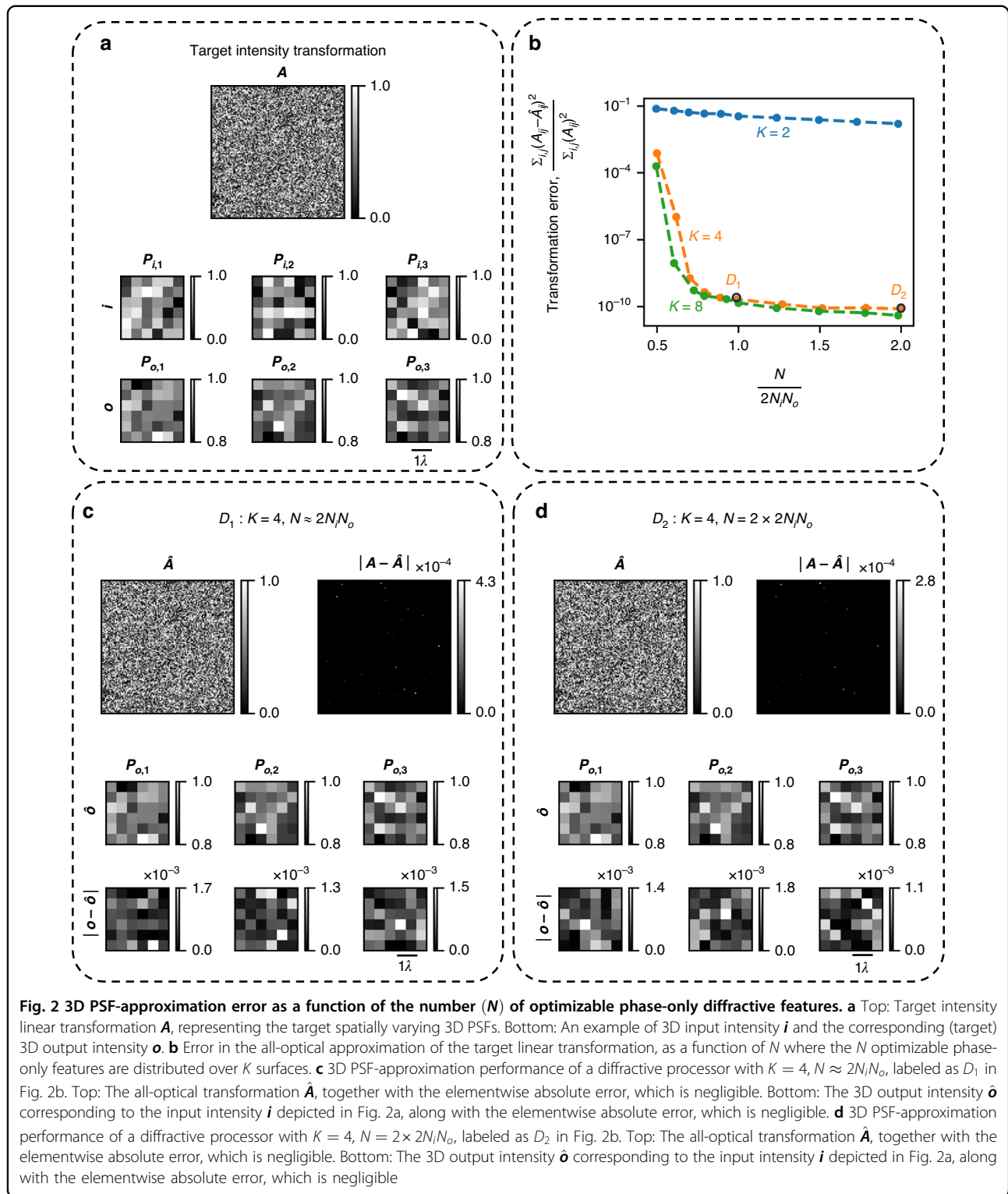
emission intensities over the $N_i = C_i \times H_i \times W_i$ input voxels. The output volume is similarly discretized into N_o voxels, the intensities of which are represented by the vector \hat{o} . The diffractive processor is optimized to create an arbitrary set of N_i 3D PSFs, represented by the N_i columns of the matrix A (see the bottom-right panel of Fig. 1), so that for a given input i the output intensity distribution $\hat{o} = \hat{A}i \approx Ai$. Here, \hat{A} denotes the all-optical intensity transformation (within a scalar factor) performed by the spatially incoherent diffractive processor. In other words, the diffractive network \hat{A} is optimized to all-optically approximate an arbitrarily defined linear transformation A between the intensity distributions over the input and output volumes, i.e., $\hat{A} \approx A$ is approximated for a given set of desired spatially varying incoherent PSFs specified by A . In our analysis, we assume spatially incoherent input light, emitted by independent light emitters (for example, fluorescent molecules) distributed within the input volume; we further assume that different point emitters at the input volume do not interact with each other and do not cause shadowing, blocking or secondary excitation of each other. Stated differently, emitter-to-emitter or object-to-object interactions within the input volume are ignored, making the spatially incoherent 3D system linear in intensity (see the “Discussion” and “Methods” sections for further details).

First, we examine the all-optical linear transformation errors, i.e., 3D PSF-approximation errors, of our diffractive processors as a function of the number (N) of optimizable phase-only diffractive features available within the optical processor. Figure 2a depicts the target (desired) linear transformation A , together with an example pair of input (i) and target (o) intensity distributions satisfying $o = Ai$. The columns of A represent the target 3D PSFs (vectorized). The elements of A are randomly and independently sampled from uniform distributions between 0 and 1—mimicking any arbitrary set of N_i spatially varying 3D PSFs, where each function is real-valued and non-negative, representing a unique/desired PSF connecting an input voxel to the output voxels. In Fig. 2b, we plot the *transformation errors*, i.e., the errors between the target transformation A and the all-optical transformations \hat{A} performed by the optimized diffractive processors with N diffractive features distributed over K successive surfaces. To clarify, each point on the interpolated curves of Fig. 2b represents a separately trained diffractive processor with the associated (K, N) design value. From the $K = 4$ and $K = 8$ curves, we can see that the transformation error between A and \hat{A} decreases rapidly to a negligible value as N approaches $2N_iN_o$; beyond $N = 2N_iN_o$ the error does not decrease further. We also note that shallower diffractive networks with, e.g., $K = 2$ successive surfaces have larger errors in approximating the target linear transformation, even

when N exceeds $2N_iN_o$, showing the importance of *depth* in a diffractive network architecture^{27–30}. These analyses indicate that, given sufficient degrees of freedom N distributed over a deeper architecture, diffractive networks can approximate arbitrary linear transformations between the input and output volumes with negligible error. Figure 2c, d further outline the performance of two $K = 4$ diffractive processors with $N \approx 2N_iN_o$ and $N = 4N_iN_o$, labeled as D_1 and D_2 in Fig. 2b, respectively. For both of these designs, the all-optical linear transformation \hat{A} representing the 3D PSFs is shown, together with the elementwise absolute differences with respect to the desired transformation, i.e., $|A - \hat{A}|$, which indicate that the errors in the approximate 3D PSFs are negligible, as desired. These figures also show the respective output 3D intensity distributions (\hat{o}) for the input intensity distribution i depicted in Fig. 2a. The corresponding absolute differences (elementwise) with respect to the target o (shown in Fig. 2a), i.e., $|o - \hat{o}|$ also reveal negligible errors in the output 3D intensities, further supporting our conclusions.

For a deeper diffractive processor architecture to achieve an accurate all-optical transformation, i.e., $\hat{A} \approx A$, the empirical convergence threshold required for N is dictated by the number of diffraction-limited voxels at the input (N_i) and the output (N_o) volumes, and the factor of 2 in this threshold, $2N_iN_o$, is due to the fact that phase-only diffractive features are used as part of the diffractive processor design. While complex-valued optimizable diffractive features would be ideal from the perspective of a 2-fold increase in the independent degrees of freedom available for a given design, phase-only feature-based processors are easier to fabricate and would present lower losses.

Next, we explore the effect of the diffraction limit of light on the approximation of arbitrary 3D PSFs by diffractive networks. We consider two parameters related to the diffraction limit: (1) plane-to-plane distance (d_{pp}) within the input and output volumes, and (2) the distances of the farthest planes within the input and output volumes from the first and the last diffractive surfaces (d_i and d_o), which dictate the input and output numerical apertures (NA) of the diffractive processor, respectively. Without loss of generality, we assume a symmetric architecture where $d_i = d_o$ and the interplane distances d_{pp} within the input and output volumes are the same; see the top panel of Fig. 3. As for the diffractive processor architecture, we assume $N = 4N_iN_o$ optimizable phase-only diffractive features distributed over $K = 4$ surfaces. In Fig. 3a, we show the trends of the transformation error as a function of d_{pp} , parameterized by the corresponding values of $d_i = d_o$. For a given $d_i = d_o$ value, e.g., 10.5λ , the transformation error increases monotonically as d_{pp} decreases beyond the axial resolution set by the input/



output NA of the processor. For a larger $d_i = d_o = 21.0\lambda$ (i.e., a smaller NA), the axial resolution of the diffractive processor is even more limited, and the onset of the monotonic error increase occurs at a larger d_{pp} value

compared to the $d_i = d_o = 10.5\lambda$ case—as expected. This dependence on NA can be further explained by plotting the transformation error as a function of $d_i = d_o$ for a given d_{pp} , as shown in Fig. 3b. For $d_{pp} = 3.0\lambda$, the

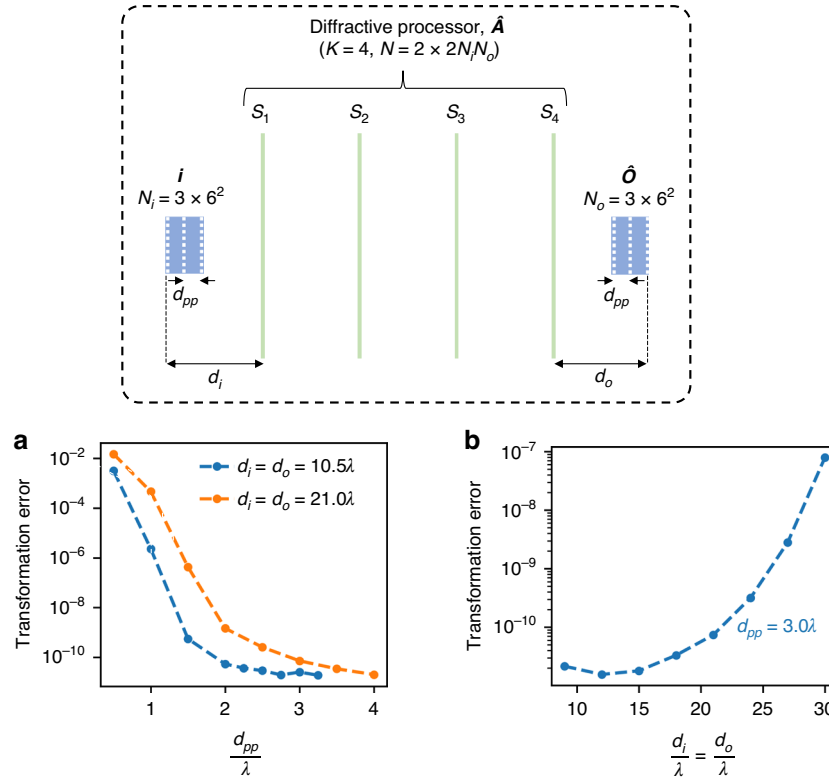


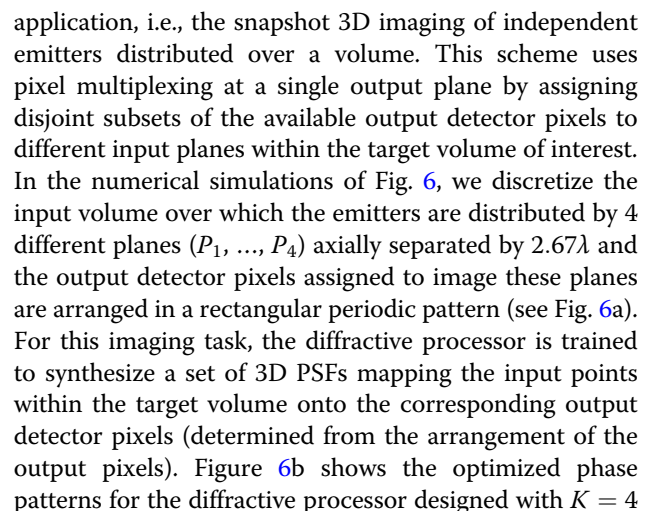
Fig. 3 Effect of diffraction limit on the 3D PSF-approximation error. **a** 3D PSF-approximation error as a function of plane-to-plane distance d_{pp} within the input and output volumes, while the distances of the first input plane (d_i) and the last output plane (d_o) from the diffractive processor are kept constant. The two curves correspond to two different values of $d_i = d_o$. **b** 3D PSF-approximation error as a function of $d_i = d_o$, while the plane-to-plane distance d_{pp} is kept constant

transformation error increases rapidly as $d_i = d_o$ increases beyond 21.0λ , which results in an axial resolution limit larger than 3λ (i.e., $\frac{2\lambda}{NA^2} \approx 3.05\lambda$ where $NA \approx 0.81$ for $d_i = d_o = 21\lambda$ and a diffractive layer width of $W \approx 57\lambda$; see the “Methods” section).

We proceed to investigate the dependence of 3D PSF-approximation error on the discretization of the diffractive surface phase features. We quantify the precision with which the phase of the optimized surfaces can be realized based on the phase bit depth, where a bit depth of b corresponds to 2^b discrete levels of phase modulation between 0 and 2π (e.g., $b = \infty$ implies continuous phase modulation). Additionally, we examine how deviations from the assumed training bit depth affect the all-optical transformation accuracy of a diffractive network, by evaluating a network trained with a bit depth of b_{tr} under various phase bit depths b_{te} in the testing stage. In Fig. 4a, the target transformation \mathbf{A} is shown on the left, while on the right, we plot the transformation error as a function of b_{te} for five different diffractive processor designs, each trained to all-optically perform \mathbf{A} using a distinct phase bit depth b_{tr} . For a given diffractive design trained with b_{tr} , the transformation error remains nearly constant as long as $b_{te} \geq b_{tr}$.

However, when $b_{te} < b_{tr}$, the transformation error increases, highlighting the impact of the phase quantization. Figure 4a further reveals that the implementation of phase modulation with large bit depths is useful if the training is performed assuming an equal or higher phase bit depth. In Fig. 4b, we also present the all-optical linear transformation $\hat{\mathbf{A}}$ corresponding to $b_{te} = b_{tr}$ for these designs, alongside the elementwise absolute errors with respect to the desired transformation, i.e., $|\mathbf{A} - \hat{\mathbf{A}}|$. As expected, the error is significant when $b_{tr} = b_{te} = 4$, but it decreases as $b_{tr} = b_{te}$ increases; e.g., the maximum absolute error reduces to ~ 0.02 for $b_{tr} = b_{te} = 12$.

Figure 5 further illustrates the collective impact of phase bit depth in conjunction with other design hyperparameters (e.g., the number of phase-only diffractive surfaces K and optimizable phase-only spatial features N) on the fidelity of all-optical 3D intensity transformations with spatially incoherent diffractive networks. In Fig. 5a, the left panel displays the target transformation \mathbf{A} , while the right panel plots the transformation error as a function of bit depth ($b_{tr} = b_{te}$) for diffractive designs with different (K, N) values. As expected, the transformation error decreases with increasing bit depth, demonstrating



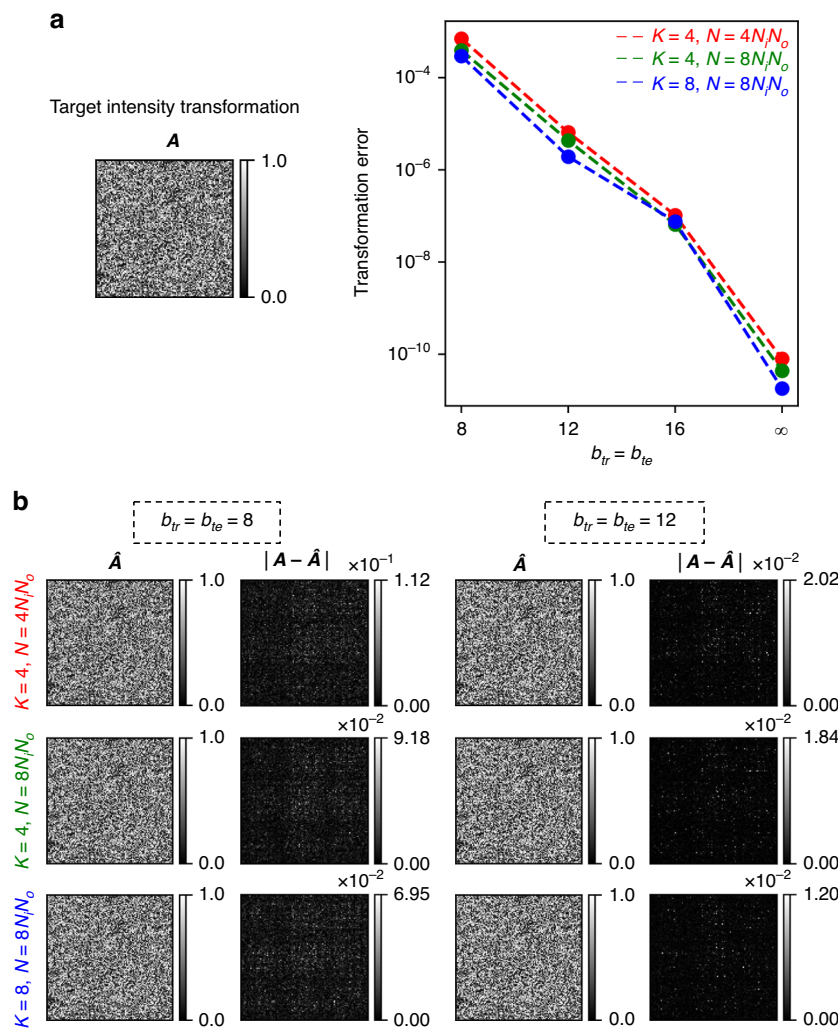


Fig. 5 Impact of phase bit depth and design configuration (K, N) on the 3D PSF-approximation error. a (Left) The target intensity transformation **A**, the columns of which represent the target (desired) 3D PSFs that are spatially varying. (Right) The transformation error, as a function of the bit depth $b_{tr} = b_{te}$ for several design configurations (distinguished by different values of K and N). **b** The all-optical transformation \hat{A} , together with the elementwise absolute error $|A - \hat{A}|$ for the designs with $b_{tr} = b_{te} = 8$ and $b_{tr} = b_{te} = 12$

successive surfaces, and the resulting imaging performance with test objects is shown in Fig. 6c. The emission intensities over the input volume are mapped onto the corresponding intensities over a single output/detector plane. Demultiplexing of these raw output pixels at the detector array, assigned to different axial input planes, reveals the emission intensities over each input plane with negligible error. This snapshot 3D imaging of incoherent emitters within an input volume of interest does not require any axial scanning or digital image reconstruction steps^{31,32}, and it only involves the rearrangement of the output detector pixel values, which achieves axial demultiplexing from a single output image.

The presented 3D information processing framework can also synthesize *spectrally* and *spatially* varying incoherent

PSFs, which can enable *snapshot 3D multispectral imaging*. In the numerical simulations illustrated in Fig. 7, three distinct types of emitters, emitting at three different wavelengths (e.g., three different fluorophores) are assumed to be distributed over the input volume; see Fig. 7a. At the output plane corresponding to a detector array, three pixels are assigned to each input voxel: one for each emission wavelength. Demultiplexing of the output pixels assigned to different input planes and emission wavelengths (i.e., *axial and spectral* demultiplexing) reveals the multispectral emission intensities over each input plane; see Fig. 7c. Note that in such a snapshot 3D multispectral imager, the same diffractive network processes all the spectral components, simultaneously outputting the spectral images at the corresponding pixels. The separate demonstrations of 3D

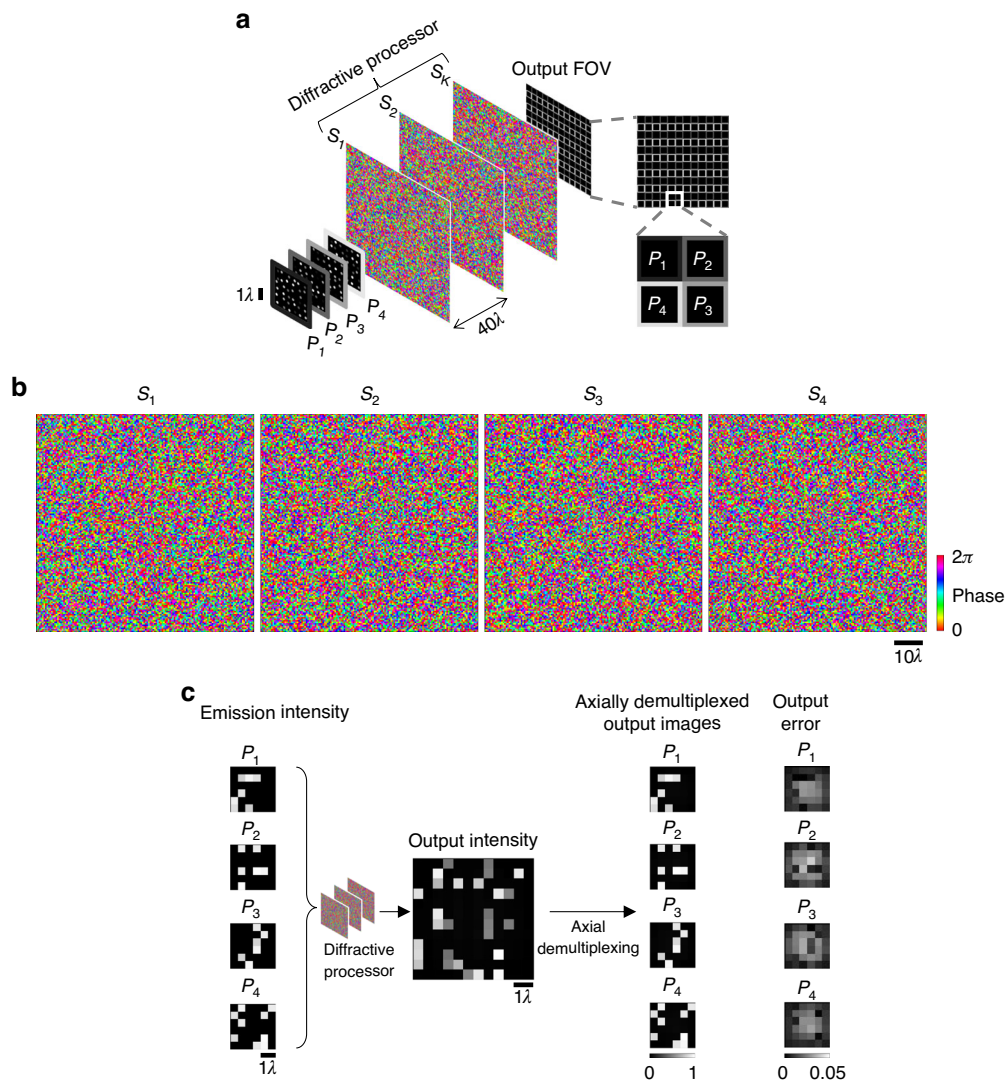
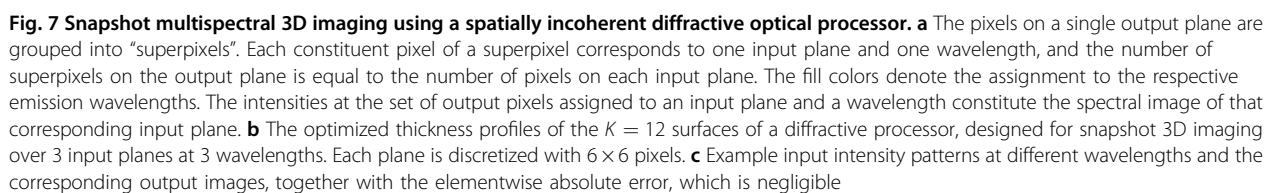
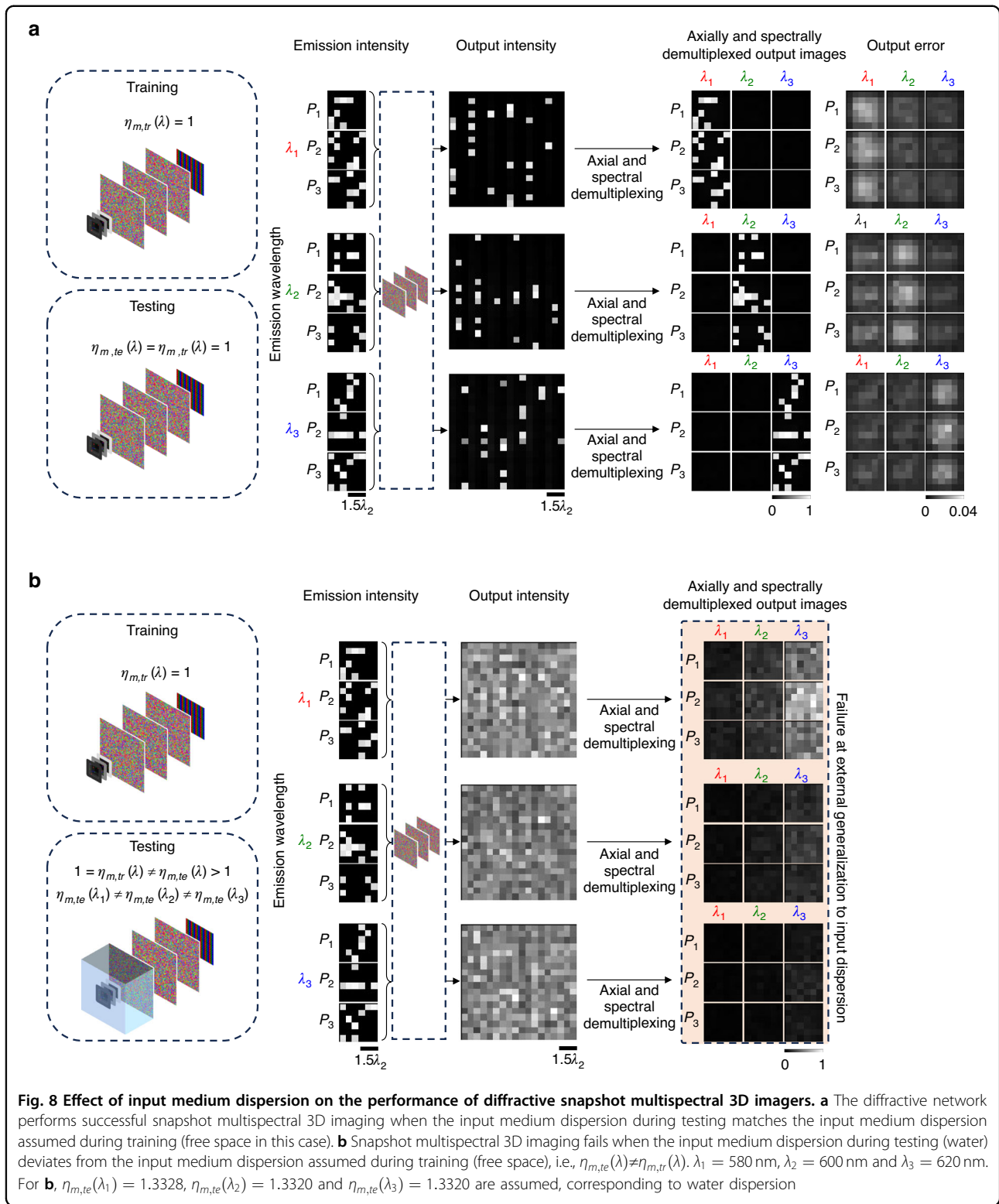


Fig. 6 Snapshot 3D imaging using a spatially incoherent diffractive optical processor. **a** The pixels on a single output plane are grouped into “superpixels”. Each constituent pixel of an output superpixel corresponds to one input plane, and the number of superpixels on the output plane is equal to the number of pixels on each input plane. The shaded outlines around the pixels denote the assignment to the respective input planes. The intensities at the set of output pixels assigned to an input plane constitute the image of that input plane. **b** The optimized phase profiles of the $K = 4$ surfaces of a diffractive processor, designed for snapshot 3D imaging over four input planes. **c** Each input plane is discretized with 6×6 diffraction-limited pixels, with a distinct emitter configuration in each plane. An example input intensity pattern at the input volume and the corresponding output image, together with the elementwise absolute error, which is negligible

imaging at different wavelengths in Fig. 7c further emphasize the negligible cross talk at the output pixels, i.e., when only one type of emitter (corresponding to one emission wavelength) is present, there is negligible leakage signal at the pixels dedicated to the other wavelengths—as desired. These results demonstrate the accurate approximation of a desired set of spatially and spectrally varying 3D incoherent PSFs required for snapshot 3D multispectral imaging of a volume using a single output detector array (without any axial scanning, spectral filters or digital image reconstruction algorithms).

Next, in Figs. 8 and 9, we explore the effect of the refractive index dispersion $\eta_m(\lambda)$ of the input medium on the performance of snapshot 3D multispectral imagers; here η_m is the refractive index of the medium immersing the incoherent emitters. For Fig. 8, we assume that the input medium dispersion is unknown in our design; hence, the diffractive imager is trained assuming $\eta_{m,tr}(\lambda) = 1$ at all λ . However, after its training/design, we blindly compare its performance for two test cases: (1) the medium dispersion follows the training, i.e., $\eta_{m,te}(\lambda) = \eta_{m,tr}(\lambda) = 1$ for all λ ; and (2) the medium dispersion





deviates from the training, i.e., $\eta_{m,te}(\lambda) \neq \eta_{m,tr}(\lambda)$ for all λ . For these numerical analyses, we assumed the operation wavelengths to be in the visible part of the spectrum (i.e., $\lambda_1 = 580$ nm, $\lambda_2 = 600$ nm, $\lambda_3 = 620$ nm) and water to be

the dispersive input medium ($\eta_m(\lambda_1) = 1.3328$, $\eta_m(\lambda_2) = 1.3320$, $\eta_m(\lambda_3) = 1.3320$). Figure 8a shows that the diffractive imager works with negligible error when the input medium dispersion follows the training (free space), i.e.,

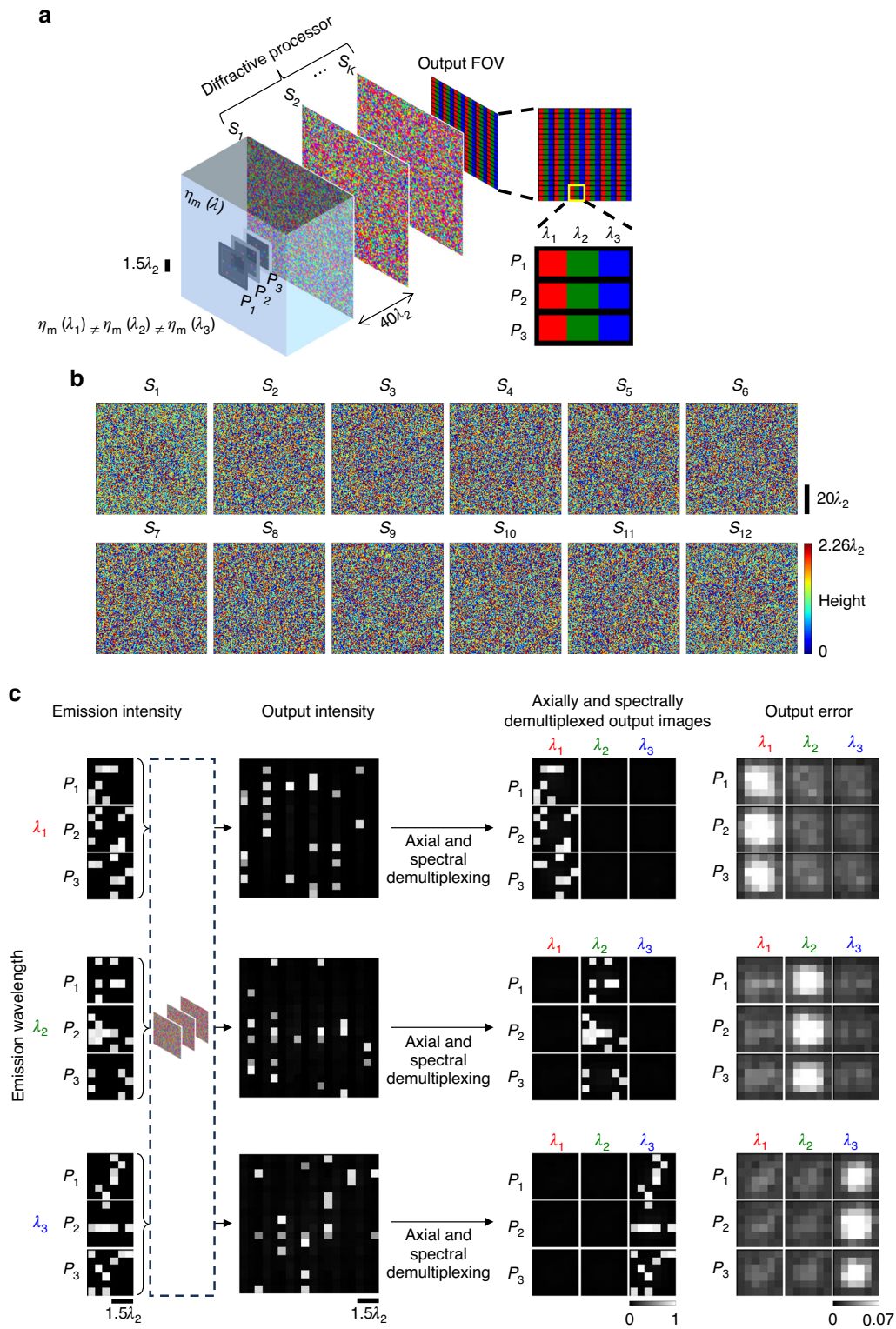


Fig. 9 Snapshot multispectral 3D imaging of emitters within a dispersive medium using a spatially incoherent diffractive optical processor, where $\eta_{m,te}(\lambda) = \eta_{m,tr}(\lambda)$. **a** Similar to Fig. 7a, except the emitters are assumed to be immersed in a dispersive medium (water). **b** The optimized thickness profiles of the $K = 12$ surfaces of a diffractive processor, designed for snapshot 3D imaging over 3 input planes *immersed within water*. **c** Example water-immersed input intensity patterns at different wavelengths and the corresponding output images, together with the elementwise absolute error, which is negligible. For this figure, $\lambda_1 = 580$ nm, $\lambda_2 = 600$ nm, $\lambda_3 = 620$ nm and $\eta_m(\lambda_1) = 1.3328$, $\eta_m(\lambda_2) = 1.3320$, $\eta_m(\lambda_3) = 1.3320$, corresponding to water dispersion

$\eta_{m,te}(\lambda) = \eta_{m,tr}(\lambda) = 1$. On the other hand, if the same diffractive design is tested when the input medium is replaced with water, deviating from the training assumption ($\eta_{m,te}(\lambda) \neq \eta_{m,tr}(\lambda)$), the diffractive imager fails in its desired transformation accuracy due to the lack of external generalization to different input media; see Fig. 8b. However, the prior knowledge of the input medium dispersion corresponding to water can be incorporated into the training stage of snapshot multi-spectral 3D imagers to overcome this failure. In Fig. 9, we report the performance of a diffractive imager trained under the assumption of a dispersive input medium (water), which demonstrates successful snapshot multi-spectral 3D imaging when tested under the same assumption of water immersion, i.e., $\eta_{m,te}(\lambda) = \eta_{m,tr}(\lambda)$.

Discussion

The application of conventional PSF engineering techniques for 3D information processing involves trade-offs among design flexibility, hardware complexity, and computational demands. For instance, microlens arrays are used in light-field microscopy to encode the depth information into 2D measurements; however, they sacrifice lateral resolution in return for depth information and require extensive digital postprocessing that partially limits real-time applications. Multifocal microscopy, on the other hand, typically relies on bulky multi-detector setups, adding to optical system complexity. Hybrid methods that combine optical setup modifications with iterative algorithms, such as structured illumination microscopy and Fourier ptychography, enhance imaging capabilities at the expense of speed and simplicity. Similarly, pupil engineering approaches (such as tetrapod PSFs and coded apertures) remain confined to laterally *invariant* PSFs and are also limited by the speed of digital postprocessing. Most notably, *none of these approaches enable the engineering of spatially varying arbitrary sets of 3D PSFs*. In contrast, diffractive optical processors reported in this work are shown to passively synthesize arbitrary 3D PSFs within a spatially incoherent framework, enabling snapshot 3D imaging while eliminating the need for digital postprocessing. Moreover, they enable postprocessing-free spectral 3D imaging without relying on spectral filters or 3D scanning. Subject to the diffraction limit of light, our designs avoid the resolution trade-offs associated with microlens arrays or lateral invariance of coded apertures. This blend of universal 3D PSF programmability, spectral multiplexing capability, and passive operation positions diffractive optical processors as a promising platform for real-time and high-throughput 3D information processing.

In the numerical analyses presented so far, we assumed that there is no interaction among incoherent emitters of interest. Stated differently, the independent emitters within the target volume at the input do not influence

each other, e.g., they do not excite, shadow or block other emitters. If this assumption is violated due to, for example, some emitters scattering or absorbing the emissions of other emitters, the optical system becomes nonlinear from the perspective of input information encoding and cannot be represented by a linear optical forward model ($\mathbf{o} = \mathbf{A}\mathbf{i}$). In that case, the output 3D intensity patterns, \mathbf{o} , become a nonlinear function of \mathbf{i} , and the nature of this nonlinear transformation function depends on the specific distribution and the complex-valued scattering potential of the input object volume, which altogether make the problem significantly more difficult to model due to *emitter-to-emitter coupling*, which is at the heart of nonlinear information encoding. The functional form of such a system becomes object-dependent³³, which means that every unique 3D object topology (k) will have a different nonlinear transformation function, i.e., $f_k(\mathbf{i})$, at the output if the emitter-to-emitter coupling is not negligible. For an input volume where the emitters exhibit cross-coupling with each other, the specific 3D topology (k) of this volume (dictated by, e.g., the cross-coupling strengths, refractive index distributions, etc.) would change the functional form of the nonlinear transformation, $f_k(\mathbf{i})$; in general, we have $f_k(\mathbf{i}) \neq f_m(\mathbf{i})$ for $k \neq m$. These arguments only apply if there is considerable cross-talk among the incoherent emitters of interest; however, weakly scattering and low-density independent emitters located within a uniform and transparent medium would follow the assumptions of our forward model and can be modeled through spatially varying 3D incoherent PSFs represented by our linear system, $\mathbf{o} = \mathbf{A}\mathbf{i}$.

More specifically, in our forward model, we make two fundamental assumptions that are also implicit in most 3D imaging techniques. First, the excitation or illumination of a given emitter is independent of the presence or absence of other emitters. In other words, the excitation/illumination beam remains largely unaltered by the emitters themselves, neglecting potential shadowing effects³⁴. Second, the emitted light of each point source (e.g., fluorescence emission) is assumed to propagate without undergoing further scattering by other emitters or the surrounding sample, neglecting phenomena such as self-absorption³⁵. These assumptions enable a linear model, where the total output intensity distribution is the sum of the contributions from individual emitters. While these assumptions would restrict our method to weakly scattering media, leading to performance degradation in highly scattering environments, similar assumptions underpin most established 3D fluorescence microscopy techniques, including confocal and light-sheet microscopy. In 3D incoherent imaging, it is typically assumed that the excitation or illumination beam traverses the sample with minimal absorption or scattering by fluorophores/emitters before reaching the focal plane. This assumption holds for weakly absorbing or sparsely labeled specimens but breaks

down in dense or highly absorbing or scattering samples, where attenuation of the excitation beam becomes significant, resulting in sample-dependent and unknown aberrations. Likewise, the emitted light (e.g., fluorescence) is generally assumed to reach the detector without substantial scattering or absorption by the sample or other fluorophores. While this assumption is valid for optically cleared or thin samples with minimal refractive index variations, it fails in thick, dense, or uncleared tissues, where multiple scattering and reabsorption can introduce signal distortions. Similar to these established 3D imaging techniques, our proposed methods would also encounter challenges in highly scattering media or densely labeled samples that violate the underlying assumptions. In fact, such assumptions are not unique to incoherent imaging or our reported methods in this manuscript. In 3D coherent imaging techniques such as optical diffraction tomography or optical coherence tomography, the first Born approximation or Rytov approximation is used to simplify the forward model for the scattered field by substituting the total field with the incident field³⁶, which implies an assumption of weak scattering. Such approximations ignore multiple scattering and higher-order interactions, enabling accurate reconstruction when refractive index variations are relatively small but leading to errors when multiple scattering becomes significant. In summary, the assumptions behind our reported methods align well with those of the established 3D imaging methodologies, maintaining consistency with the broader field of 3D optical imaging.

The large 3D PSF approximation error for $K = 2$ in Fig. 2b emphasizes the importance of structural depth, in terms of the number of successive surfaces, on the performance of diffractive optical processors. Previous works on diffractive processors reported a similar phenomenon, where shallower diffractive networks suffer from relatively larger approximation errors for different desired tasks because of the dominance of the ballistic photons^{28,30} at the output plane/volume. With sufficient structural depth, this error is well mitigated, as seen by the small gap between the $K = 4$ and $K = 8$ curves in Fig. 2b.

It is important to emphasize that the thresholds for the number of optimizable diffractive features (N) and the number of diffractive surfaces (K), as reported in Fig. 2b, represent strict requirements for implementing *arbitrary* linear transformations corresponding to spatially varying arbitrary 3D PSFs. However, for task-specific optical transformations, these requirements could be significantly relaxed. In practice, the optimal values of K , N , and also the phase bit depth, depend on the specific target transformation to be realized and the acceptable level of approximation error at the output. Therefore, these should be treated as hyperparameters and selected through an optimization process that is tailored to the desired optical task at hand.

Regarding the demonstration of snapshot multispectral 3D imaging reported in Figs. 7–9, it should be noted that all the pixels at the output plane are assumed to be identical with no wavelength specificity, and there is no spectral filtering involved. For a given wavelength, the diffractive processor is optimized to route the photons at the designated pixels and away from the other pixels (eliminating spectral cross-talk), as shown in the raw “Output intensity” and “Axially and spectrally demultiplexed output images” in Figs. 7c, 8a, and 9c. Accordingly, when independent emitters of different types (i.e., emitting at different wavelengths) are present in the same input volume, such a snapshot 3D multispectral imager simultaneously processes all the spectral components of the 3D emitters within the input volume to output the spectral images at the corresponding pixels of the output detector array.

Another important feature of the presented diffractive processors is that their design, i.e., the diffractive layers and the corresponding features optimized for a desired 3D optical information processing task, can be translated to different parts of the electromagnetic spectrum without redesigning the layers due to the scale invariance of the underlying formalism based on Maxwell’s equations. Furthermore, the spectral engineering of the spatially varying 3D PSFs that is achieved using diffractive processors (e.g., for the snapshot multispectral 3D imaging reported in Figs. 7–9) does *not* rely on the specific properties or optimization of the material dispersion; the dispersion resulting from free-space propagation of optical waves suffices in the spectral engineering of spatially varying 3D PSFs even if the material dispersion is negligible with a relatively flat refractive index as a function of wavelength²⁹. Therefore, the conclusions of our analyses are broadly applicable to various materials of interest that operate at different parts of the electromagnetic spectrum without the need for redesigning the task-specific optimized diffractive features.

Regarding the practical implementations of 3D PSF engineering with diffractive processors, fabrication technologies for high-resolution phase layers are already well-established, with techniques like electron-beam lithography, nanoimprinting, and two-photon polymerization enabling nanofabrication with a resolution as small as 25 nm^{37–42}. However, the primary challenge lies in the alignment of multiple layers at such a small scale. In designs with cascaded diffractive surfaces, accumulated misalignments such as shifts, tilts, and rotations can lead to performance degradations. Potential solutions are also emerging to address these alignment challenges. For example, monolithic fabrication, integrating multiple surfaces into a single 3D structure, was reported for the fabrication of a multi-layer diffractive network on the end facet of an optical fiber⁴³. Future progress in self-assembly methods may further simplify the integration and 3D alignment of diffractive surfaces for improved performance^{44–46}. Misalignment-aware training of diffractive networks can also

be used to improve the resilience of the designed optical hardware against such misalignments and relax the alignment requirements⁴⁷; similar strategies can also be used to mitigate the impact of fabrication imperfections. While challenges remain, these advancements promise robust and scalable multi-layer diffractive processors for high-density 3D optical information processing at the diffraction limit of light.

We believe that the results presented here lay the groundwork for 3D optical information processing systems with incoherent diffractive processors. As demonstrated through our numerical analyses, diffractive processors can be optimized to process 3D spatial information at multiple wavelengths through desired sets of spatially and spectrally programmed incoherent PSFs, covering various applications in imaging and sensing with unique capabilities beyond traditional spatially invariant free-space optics-based processors.

Materials and methods

Optical forward model of spatially incoherent diffractive networks

A 3D distribution of monochrome emitters (e.g., weak scatterers within a volume) can be modeled by a three-dimensional complex-valued function \tilde{i} , representing the amplitude and phase of the emitted (secondary) waves at a wavelength of λ . The complex amplitude \tilde{o} of the corresponding output waves of a linear optical processor, described by the impulse response function h , can be written as:

$$\tilde{o}(x, y, z) = \iiint h(x, y, z; x', y', z') \tilde{i}(x', y', z') dx' dy' dz' \quad (1)$$

Here (x', y', z') and (x, y, z) denote the spatial coordinates within the input and output volumes, respectively. We use the symbol \sim over variables to denote *coherent* (complex-valued) optical fields. If these optical fields are sampled at intervals (laterally δ and axially d_{pp}) that are sufficiently small to preserve the diffraction-limited spatial variations, one can write:

$$\tilde{o}(l, m, n) = \sum_{l', m', n'} h(l, m, n; l', m', n') \tilde{i}(l', m', n') \quad (2)$$

Here, l, m, n, l', m', n' refer to discrete indices such that $\tilde{o}(l, m, n) \triangleq \tilde{o}(l\delta, m\delta, nd_{pp})$ and $\tilde{i}(l', m', n') \triangleq \tilde{i}(l'\delta, m'\delta, n'd_{pp})$. The instantaneous 3D output intensity can be written as:

$$|\tilde{o}(l, m, n)|^2 = \sum_{l', m', n', l'', m'', n''} h(l, m, n; l', m', n') h^*(l, m, n; l'', m'', n'') \tilde{i}(l', m', n') \tilde{i}^*(l'', m'', n'') e^{j(\varphi(l', m', n') - \varphi(l'', m'', n''))} \quad (3)$$

where φ is the phase of the input wave, i.e., $\tilde{i} = |\tilde{i}|e^{j\varphi}$, and h^* denotes the complex conjugate of h . The time-averaged

output intensity can be written as:

$$\begin{aligned} O(l, m, n) &= \langle |\tilde{o}(l, m, n)|^2 \rangle \\ &= \sum_{l', m', n', l'', m'', n''} h(l, m, n; l', m', n') h^*(l, m, n; l'', m'', n'') \\ &\quad \langle \tilde{i}(l', m', n') \tilde{i}^*(l'', m'', n'') \rangle e^{j\Delta\varphi} \end{aligned} \quad (4)$$

where $\langle \cdot \rangle$ denotes time-average operation and $\Delta\varphi = \varphi(l', m', n') - \varphi(l'', m'', n'')$ is the phase difference between any arbitrary pairs of emitters within the input volume. For a spatially incoherent 3D system, the phase differences $\Delta\varphi$ between any pair of volumetric emitters (separated from each other by a 3D grid that follows the diffraction limit of light) vary randomly over time. Stated differently, for a stationary spatial distribution of independent emitters, each $\Delta\varphi = \varphi(l', m', n') - \varphi(l'', m'', n'')$ between a pair of emitters vary randomly between 0 and 2π over time, yielding $\langle e^{j\Delta\varphi} \rangle = 0$ for $(l', m', n') \neq (l'', m'', n'')$. As a result of this, Eq. 4 can be written as:

$$\begin{aligned} O(l, m, n) &= \sum_{l', m', n'} |h(l, m, n; l', m', n')|^2 \\ \langle |\tilde{i}(l', m', n')|^2 \rangle &= \sum_{l', m', n'} H(l, m, n; l', m', n') I(l', m', n') \end{aligned} \quad (5)$$

where $I = \langle |\tilde{i}|^2 \rangle$ is the time-averaged input intensity of the sample volume of interest and $H(l, m, n; l', m', n') = |h(l, m, n; l', m', n')|^2$ describes the spatially incoherent 3D PSFs, i.e., the 3D output intensity distribution for a point emitter at (l', m', n') . Equation 5 can be written as a matrix equation $\mathbf{o} = \mathbf{A}\mathbf{i}$ with a one-to-one correspondence between $H(l, m, n; l', m', n')$ and the elements of \mathbf{A} , where \mathbf{o} and \mathbf{i} are the vector representations of O and I , respectively.

In our numerical forward model, we assumed that the input volume is axially discretized by C_i planes $\{P_{i,n'}\}_{n'=1}^{C_i}$, each of which is laterally discretized by $H_i \times W_i$ pixels, giving rise to $N_i = H_i \times W_i \times C_i$ input voxels. Similarly, the output volume is also discretized into $N_o = H_o \times W_o \times C_o$ voxels over C_o planes $\{P_{o,n}\}_{n=1}^{C_o}$; see Fig. 1. In our notation below, we separate the axial dependence of the quantities with a semicolon for better clarity (e.g., $O(l, m, n) = O(l, m; n)$). Under the assumption of negligible emitter-to-emitter coupling, the total intensity at the output plane $P_{o,n}$ can be written as:

$$O(l, m; n) = \sum_{n'=1}^{C_i} O_{n'}(l, m; n) \quad (6)$$

where $O_{n'}(l, m; n)$ is the contribution of the emitters on $P_{i,n'}$ to $O(l, m; n)$, simulated through the spatially incoherent propagation of the emission intensity on $P_{i,n'}$,

i.e., $I(l', m'; n')$, as follows:

$$\begin{aligned} O_{n'}(l, m; n) &= \langle |\mathcal{D}_{n' \rightarrow n} \{ \sqrt{I(l', m'; n')} e^{j\varphi_r(l', m'; n')} \} |^2 \rangle \\ &= \lim_{N_\varphi \rightarrow \infty} \frac{1}{N_\varphi} \sum_{r=1}^{N_\varphi} |\mathcal{D}_{n' \rightarrow n} \{ \sqrt{I(l', m'; n')} e^{j\varphi_r(l', m'; n')} \} |^2 \end{aligned} \quad (7)$$

Here $\mathcal{D}_{n' \rightarrow n} \{ \cdot \}$ denotes the spatially coherent optical field propagation from the input plane $P_{i, n'}$ to the output plane $P_{o, n}$ through the diffractive processor. The spatial incoherence of the overall emissions is modeled by the averaging operation $\langle \cdot \rangle$ over all the instances of random input phase distributions $\varphi(l', m'; n')$, approximated by averaging over a large number N_φ of random phase values $\varphi_r(l', m'; n')$ where $\varphi_r(l', m'; n') \sim \text{Uniform}(0, 2\pi)$ ^{30,48,49}. The propagation $\mathcal{D}_{n' \rightarrow n} \{ \cdot \}$ of the complex optical fields $\sqrt{I(l', m'; n')} e^{j\varphi_r(l', m'; n')}$ through the diffractive processor comprises a series of spatial modulations of the field by the diffractive surfaces, interleaved by the free-space propagation between successive diffractive surfaces. The optical field incident on a diffractive surface is locally modulated by the diffractive features. Throughout this paper, we assume passive surfaces with *phase-only* diffractive features, i.e., only the phase delays, not the absorption, of these spatial features are trainable. In other words, if the optical field incident on a surface is $\tilde{u}(x, y)$, then the field leaving the surface would be $\tilde{u}(x, y) e^{j\phi_s(x, y)}$ where the local phase delay $\phi_s(x, y)$ of the surface is related to its thickness $t_s(x, y)$ as $\phi_s = \frac{2\pi}{\lambda} (\eta - 1) t_s$; here, η is the refractive index of the diffractive material at the wavelength λ ⁵⁰.

Free-space propagation of an optical field between successive diffractive surfaces is simulated using the angular spectrum method¹, according to which the propagation of an optical field by distance d can be calculated as follows:

$$\tilde{u}(x, y; z_0 + d) = \mathcal{F}^{-1} \left\{ \mathcal{F} \{ \tilde{u}(x, y; z_0) \} \times H(f_x, f_y; d) \right\} \quad (8)$$

where $\tilde{u}(x, y; z_0)$ is the optical field distribution over the $z = z_0$ plane, \mathcal{F} (\mathcal{F}^{-1}) is the two-dimensional Fourier (Inverse-Fourier) transform and $H(f_x, f_y; d)$ is the transfer function for a propagation of distance d through free-space:

$$H(f_x, f_y; d) = \begin{cases} e^{j\frac{2\pi}{\lambda} d \sqrt{1 - (\lambda f_x)^2 - (\lambda f_y)^2}}, & f_x^2 + f_y^2 < 1/\lambda^2 \\ 0, & \text{otherwise} \end{cases} \quad (9)$$

In our numerical simulations, the fields/intensities were discretized using $\delta \approx 0.53\lambda$ both along x and y , e.g.,

$\tilde{u}(l, m) \triangleq \tilde{u}(l\delta, m\delta)$ and sufficiently zero-padded before evaluating the Fourier transform, as in Eq. 8, using the Fast Fourier Transform (FFT) algorithm.

The thickness $t_s(l, m) \triangleq t_s(l\delta, m\delta)$ values of the N diffractive features (distributed over K surfaces) were optimized to all-optically perform the desired transformation of the 3D input intensity distribution. In Figs. 2 and 3, to keep the connectivity between successive diffractive layers¹⁹ the same across the trained diffractive networks with different N (resulting in different layer widths $W = \sqrt{\frac{N}{K}}\delta$ for the same K), the layer-to-layer separation was set as $d = \frac{W\delta}{\lambda} \sqrt{1 - \left(\frac{\lambda}{2\delta}\right)^2}$.

Intensity linear transformations by a spatially incoherent diffractive optical processor

If the 3D input and output intensity distributions of a diffractive processor are arranged into two vectors $\mathbf{i} \in \mathbb{R}_{\geq 0}^{N_i}$ and $\mathbf{o}' \in \mathbb{R}_{\geq 0}^{N_o}$ where $N_i = C_i \times H_i \times W_i$ and $N_o = C_o \times H_o \times W_o$ are the numbers of voxels within the respective volumes, then we have:

$$\mathbf{o}' = \mathbf{A}' \mathbf{i} \quad (10)$$

where \mathbf{A}' is the all-optical intensity transformation performed by the diffractive processor, the columns of which represent the (vectorized) 3D PSFs. \mathbf{A}' can be computed by propagating the N_i unit impulse functions located at different input voxels through the processor to the output volume, and stacking the corresponding vectorized output intensities. In other words,

$$\mathbf{A}' = \left[\mathbf{o}'_1 | \mathbf{o}'_2 | \cdots | \mathbf{o}'_{N_i} \right] \quad (11)$$

Here \mathbf{o}'_q ($q = 1, \dots, N_i$) are the output intensity vectors corresponding to the input intensity vectors \mathbf{i}_q where $\mathbf{i}_q[l] = 1$ if $l = q$ and 0 otherwise.

Optimization of spatially incoherent diffractive optical processors

To train the diffractive processors to perform a linear transformation $\hat{\mathbf{A}} \approx \mathbf{A}$, the following loss function was minimized using gradient descent:

$$\mathcal{L} = \frac{\sum_{q=1}^{N_i} \sum_{p=1}^{N_o} (\mathbf{A}[p, q] - \hat{\mathbf{A}}[p, q])^2}{\sum_{q=1}^{N_i} \sum_{p=1}^{N_o} (\mathbf{A}[p, q])^2} \quad (12)$$

Here $\hat{\mathbf{A}} = \sigma_A \mathbf{A}'$ is the scaled all-optical intensity transformation of the diffractive processor and

$$\sigma_A = \frac{\sum_{q=1}^{N_i} \sum_{p=1}^{N_o} \mathbf{A}[p, q] \mathbf{A}'[p, q]}{\sum_{q=1}^{N_i} \sum_{p=1}^{N_o} (\mathbf{A}'[p, q])^2}$$

For the imaging applications depicted in Figs. 6–9, the target linear transformation A was composed of Kronecker delta functions between the input voxels and the corresponding output pixels. In other words, $A[p, q] = 1$ if and only if the input voxel q is mapped to the output pixel p .

The thickness t_S of the diffractive features at each layer was confined between zero and a maximum value t_{\max} by using a latent variable t_{latent} :

$$t_S = \frac{t_{\max}}{2} \times [\sin(t_{\text{latent}}) + 1] \quad (13)$$

Here t_{latent} is the underlying variable, which was optimized for each diffractive feature. We chose $t_{\max} \approx \frac{\lambda}{\eta-1}$, which corresponds to a phase modulation depth of 2π . The diffractive processor models were implemented and trained using PyTorch (v1.10)⁵¹. For the numerical simulations, unless otherwise stated, we assumed $\lambda = 750 \mu\text{m}$ and $\eta = 1.6518$. For the multispectral simulations of Fig. 7, we assumed $\lambda_1 = 725 \mu\text{m}$, $\lambda_2 = 750 \mu\text{m}$, $\lambda_3 = 775 \mu\text{m}$ and the corresponding refractive indices $\eta(\lambda_1) = 1.6515$, $\eta(\lambda_2) = 1.6518$, $\eta(\lambda_3) = 1.6521$ for the diffractive material. As for the multispectral simulations of Figs. 8 and 9 in the visible part of the spectrum, the following values were used for these parameters: $\lambda_1 = 580 \text{ nm}$, $\lambda_2 = 600 \text{ nm}$, $\lambda_3 = 620 \text{ nm}$, $\eta(\lambda_1) = 1.4587$, $\eta(\lambda_2) = 1.4580$, $\eta(\lambda_3) = 1.4574$. As for t_{\max} , we chose $t_{\max} = \max_i \frac{\lambda_i}{\eta(\lambda_i)-1}$ for the multispectral simulations.

Acknowledgements

The Ozcan Research Group at UCLA acknowledges the support of the US ARO.

Author details

¹Electrical and Computer Engineering Department, University of California, Los Angeles, CA, USA. ²Bioengineering Department, University of California, Los Angeles, CA, USA. ³California NanoSystems Institute (CNSI), University of California, Los Angeles, CA, USA

Author contributions

A.O. conceived the research and initiated the project. M.S.S.R. conducted the numerical experiments, processed the data, and prepared the results. M.S.S.R. and A.O. analyzed the results and wrote the paper. A.O. supervised the project.

Data availability

All the data needed to evaluate the conclusions of this work are present in the main text. Additional data can be requested from the corresponding author.

Conflict of interest

Aydogan Ozcan serves as an Editor of the Journal. The other author declares no competing interest.

Received: 9 February 2025 Revised: 7 May 2025 Accepted: 7 May 2025
Published online: 12 June 2025

References

- Goodman, J. W. *Introduction to Fourier Optics*. (Greenwood Village: Roberts and Company Publishers, 2005).

- Khare, K., Butola, M. & Rajora, S. *Fourier Optics and Computational Imaging*. 2nd edn. (Cham: Springer, 2023), <https://doi.org/10.1007/978-3-031-18353-9>.
- Ojeda-Castañeda, J., Andrés, P. & Díaz, A. Annular apodizers for low sensitivity to defocus and to spherical aberration. *Opt. Lett.* **11**, 487–489 (1986).
- Ojeda-Castaneda, J. & Berriel-Valdos, L. R. Zone plate for arbitrarily high focal depth. *Appl. Opt.* **29**, 994–997 (1990).
- Dowski, E. R. & Cathey, W. T. Extended depth of field through wave-front coding. *Appl. Opt.* **34**, 1859–1866 (1995).
- Hell, S. W. Increasing the resolution of far-field fluorescence light microscopy by point-spread-function engineering. in *Topics in Fluorescence Spectroscopy: Nonlinear and Two-Photon-Induced Fluorescence* (ed Lakowicz, J. R.) (Springer, New York, 2002) 361–426, https://doi.org/10.1007/0-306-47070-5_9.
- Huang, B. et al. Three-dimensional super-resolution imaging by stochastic optical reconstruction microscopy. *Science* **319**, 810–813 (2008).
- Shechtman, Y. et al. Multicolour localization microscopy by point-spread-function engineering. *Nat. Photonics* **10**, 590–594 (2016).
- Shechtman, Y. Recent advances in point spread function engineering and related computational microscopy approaches: from one viewpoint. *Biophys. Rev.* **12**, 1303–1309 (2020).
- Opatovskij, N. et al. Multiplexed PSF engineering for three-dimensional multicolor particle tracking. *Nano Lett.* **21**, 5888–5895 (2021).
- Lee, S. H. et al. Increasing the storage density of a page-based holographic data storage system by image upscaling using the PSF of the Nyquist aperture. *Opt. Express* **19**, 12053–12065 (2011).
- Kim, D. et al. Advances in optical engineering for future telescopes. *Opto-Electron. Adv.* **4**, 210040 (2021).
- Hershko, E. et al. Multicolor localization microscopy and point-spread-function engineering by deep learning. *Opt. Express* **27**, 6158–6183 (2019).
- Nehme, E. et al. DeepSTORM3D: dense 3D localization microscopy and PSF design by deep learning. *Nat. Methods* **17**, 734–740 (2020).
- Bai, B. J. et al. To image, or not to image: class-specific diffractive cameras with all-optical erasure of undesired objects. *eLight* **2**, 14 (2022).
- Li, J. X. et al. Rapid sensing of hidden objects and defects using a single-pixel diffractive terahertz sensor. *Nat. Commun.* **14**, 6791 (2023).
- Bai, B. J. et al. Information-hiding cameras: optical concealment of object information into ordinary images. *Sci. Adv.* **10**, eadn9420 (2024).
- Sakib Rahman, M. S. & Ozcan, A. Integration of programmable diffraction with digital neural networks. *ACS Photonics* **11**, 2906–2922 (2024).
- Lin, X. et al. All-optical machine learning using diffractive deep neural networks. *Science* **361**, 1004–1008 (2018).
- Hu, J. T. et al. Diffractive optical computing in free space. *Nat. Commun.* **15**, 1525 (2024).
- Sakib Rahman, M. S. & Ozcan, A. Computer-free, all-optical reconstruction of holograms using diffractive networks. *ACS Photonics* **8**, 3375–3384 (2021).
- Mengu, D. & Ozcan, A. All-optical phase recovery: diffractive computing for quantitative phase imaging. *Adv. Opt. Mater.* **10**, 2200281 (2022).
- İşil, Ç. et al. Super-resolution image display using diffractive decoders. *Sci. Adv.* **8**, eadd3433 (2022).
- Bai, B. J. et al. Data-class-specific all-optical transformations and encryption. *Adv. Mater.* **35**, 2212091 (2023).
- Rahman, M. S. S. et al. Learning diffractive optical communication around arbitrary opaque occlusions. *Nat. Commun.* **14**, 6830 (2023).
- Li, J. X. et al. All-optical complex field imaging using diffractive processors. *Light* **13**, 120 (2024).
- Kulce, O. et al. All-optical information-processing capacity of diffractive surfaces. *Light* **10**, 25 (2021).
- Kulce, O. et al. All-optical synthesis of an arbitrary linear transformation using diffractive surfaces. *Light* **10**, 196 (2021).
- Li, J. X. et al. Massively parallel universal linear transformations using a wavelength-multiplexed diffractive optical network. *Adv. Photonics* **5**, 016003 (2023).
- Rahman, M. S. S. et al. Universal linear intensity transformations using spatially incoherent diffractive processors. *Light* **12**, 195 (2023).
- Wang, H. D. et al. Deep learning enables cross-modality super-resolution in fluorescence microscopy. *Nat. Methods* **16**, 103–110 (2019).
- Wu, Y. C. et al. Three-dimensional virtual refocusing of fluorescence microscopy images using deep learning. *Nat. Methods* **16**, 1323–1331 (2019).
- Li, Y. H., Li, J. X. & Ozcan, A. Nonlinear encoding in diffractive information processing using linear optical materials. *Light* **13**, 173 (2024).

34. Munck, S. et al. Challenges and advances in optical 3D mesoscale imaging. *J. Microsc.* **286**, 201–219 (2022).
35. Ge, M. Y. et al. Self-absorption correction on 2D X-ray fluorescence maps. *Sci. Rep.* **13**, 7271 (2023).
36. Born, M. & Wolf, E. *Principles of Optics: Electromagnetic Theory of Propagation, Interference and Diffraction of Light*. 7th edn. (Cambridge: Cambridge University Press, 1999).
37. Chou, S. Y., Krauss, P. R. & Renstrom, P. J. Imprint lithography with 25-nanometer resolution. *Science* **272**, 85–87 (1996).
38. Gates, B. D. et al. New approaches to nanofabrication: molding, printing, and other techniques. *Chem. Rev.* **105**, 1171–1196 (2005).
39. Manfrinato, V. R. et al. Resolution limits of electron-beam lithography toward the atomic scale. *Nano Lett.* **13**, 1555–1558 (2013).
40. Niesler, F. & Hermatschweiler, M. Two-photon polymerization—a versatile microfabrication tool. *Laser Tech. J.* **12**, 44–47 (2015).
41. Camino, F. E. et al. Single-digit nanometer electron-beam lithography with an aberration-corrected scanning transmission electron microscope. *J. Vis. Exp.* <https://doi.org/10.3791/58272> (2018).
42. Saha, S. K. et al. Scalable submicrometer additive manufacturing. *Science* **366**, 105–109 (2019).
43. Yu, H. Y. et al. All-optical image transportation through a multimode fibre using a miniaturized diffractive neural network on the distal facet. *Nat. Photonics* <https://doi.org/10.1038/s41566-025-01621-4> (2025).
44. Cho, J. et al. Fabrication of highly ordered multilayer films using a spin self-assembly method. *Adv. Mater.* **13**, 1076–1078 (2001).
45. Parviz, B. A., Ryan, D. & Whitesides, G. M. Using self-assembly for the fabrication of nano-scale electronic and photonic devices. *IEEE Trans. Adv. Packag.* **26**, 233–241 (2003).
46. Galeotti, F., Pisco, M. & Cusano, A. Self-assembly on optical fibers: a powerful nanofabrication tool for next generation “lab-on-fiber” optrodes. *Nanoscale* **10**, 22673–22700 (2018).
47. Mengu, D. et al. Misalignment resilient diffractive optical networks. *Nanophotonics* **9**, 4207–4219 (2020).
48. Yang, X. L. et al. Complex-valued universal linear transformations and image encryption using spatially incoherent diffractive networks. *Adv. Photonics Nexus* **3**, 016010 (2024).
49. Ma, G. D. et al. Unidirectional imaging with partially coherent light. *Adv. Photonics Nexus* **3**, 066008 (2024).
50. Saleh, B. E. A. & Teich, M. C. *Fundamentals of Photonics*. 3rd edn. (Hoboken: John Wiley & Sons, 2019).
51. Paszke, A. et al. PyTorch: an imperative style, high-performance deep learning library. *Proceedings of the 33rd International Conference on Neural Information Processing Systems*. (Curran Associates, Inc., Red Hook, NY, USA, 2019) p 721.